# A tri-generation system based on polymer electrolyte fuel cell and desiccant wheel – Part A: Fuel cell system modelling and partial load analysis

Behzad Najafi, Stefano De Antonellis, Manuel Intini, Matteo Zago, Fabio Rinaldi, Andrea Casalegno *

*Department of Energy, Politecnico di Milano, Via Lambruschini 4, 20156 Milano, Italy*

Received 28 July 2015
Accepted 3 October 2015
Available online 21 October 2015

## 1. Introduction

Low temperature Polymer Electrolyte Membrane Fuel Cell (PEMFC) systems, owing to their higher performance and lower emissions, have received increasing attention in the recent years as a viable alternative for meeting the electrical and thermal needs of buildings. Operational PEMFC systems have demonstrated superior performance to combustion-based generation technologies at scales from 5 kW to 2 MW, a range that includes the electrical requirements of the most of the buildings [1,2].

However, fuel cells systems are far from being flexible and partial load control may affect potential benefits significantly. In addition, exploiting cogenerated heat as primary source for thermally driven cooling process is a hard task since PEMFC rejected heat temperature is relatively low, up to 65–70 °C. Therefore, a tri-generation system based on PEMFC requires a proper technology, design and reasonably accurate simulation tools. Accordingly, part A of the present study is focused on developing a proper model of the PEMFC based system and analysing its behaviour at partial load, while Part B is focused on analysing the performance of the overall system.

Most of the previous studies have been devoted to developing models and simulating the performance of different pilot plants. Ferguson et al. [1] developed a steady-state model of a generic PEMFC cogeneration plant and studied the effect of operating strategy and fuel cell sizing on the performance of the system. Radulescu et al. [3] performed an experimental and theoretical analysis on five different PEMFC based cogeneration plants installed in France. Ersoz et al. [4] investigated the performance of different hydrocarbon reforming approaches for PEMFC based cogeneration plants. Calise et al. [5] analysed an innovative

* Corresponding author.
*E-mail address:* andrea.casalegno@polimi.it (A. Casalegno).

**Nomenclature**

*Acronyms*

| | |
|---|---|
| CHP | combined heat and power |
| DEC | desiccant evaporative cooling |
| GDL | Gas Diffusion Layer |
| HS | heat sink |
| LMTD | logarithmic mean temperature difference |
| MEA | membrane electrode assembly |
| OHM | ohmic |
| PEMFC | proton exchange membrane fuel cell |
| PES | primary energy saving |
| PrOX | Preferential Oxidation |
| SMR | Steam Methane Reforming |
| ST | storage tank |
| TER | thermal to electric ratio |
| WGS | Water Gas Shift |
| WKO | water knock out |
| W/O | without |

*Symbols*

| | |
|---|---|
| $C$ | cooling energy (MW h) |
| $E_{ID}$ | ideal voltage (V) |
| $E_a$ | activation energy (kJ mol$^{-1}$) |
| $F$ | fuel consumption (MW h) |
| $f$ | friction factor |
| $\Delta H_{298K}$ | standard enthalpy of reaction (kJ kmol$^{-1}$) |
| $I$ | current (A) |
| $k$ | rate coefficient |
| $K$ | equilibrium constant |
| LHV | low heating value (kJ kg$^{-1}$) |
| $\dot{m}$ | mass flow rate (kg s$^{-1}$) |
| $N$ | number of cells |
| $Nu$ | Nusselt number |
| $P_x$ | partial pressure of species $x$ |
| $P$ | power (kW) |
| $Pr$ | Prandtl number |
| $Q$ | thermal energy (MW h) |
| $\dot{Q}$ | time rate of heat transfer (kW) |
| $r$ | rate of reaction (mol l$^{-1}$ s$^{-1}$) |
| $R$ | universal gas constant (kJ kmol$^{-1}$ K$^{-1}$) |
| $Re$ | Reynolds number |
| $T$ | temperature (K) |
| $V$ | voltage (V) |
| $W$ | electrical energy (MW h) |

*Subscripts*

| | |
|---|---|
| $A$ | anode |
| AHU | air handling unit |
| $b$ | boiler |
| $C$ | cathode |
| cogen | cogeneration |
| el | electrical |
| th | thermal |
| tri | tri-generation |

*Greek symbols*

| | |
|---|---|
| $\eta_A$ | anodic voltage loss |
| $\eta_C$ | cathodic voltage loss |
| $\eta_{el}$ | electrical efficiency |
| $\eta_I$ | first law efficiency |
| $\eta_{th}$ | thermal efficiency |
| $\lambda_{H2}$ | anodic stoichiometric ratio |

poly-generation system based on solar heating and cooling and PEMFC technologies. Obara and Tanno [6] performed a study on PEMFC/engine combined generation plants. Obara [7] also studied the $CO_2$ emission characteristics of the same system. Nagata et al. [8] performed a quantitative analysis on $CO_2$ emissions reductions through introduction of stationary-type PEMFC systems in Japan. Hwang et al. [9] studied the implementation of a heat recovery unit for a PEMFC system; they also developed an efficient thermal control strategy for the plant.

Jovan et al. [10] performed an assessment on the actual energetic flows, and consequent electrical efficiency of a case-study PEMFC system. Najafi et al. [11,12] performed a sensitivity analysis on the steady state and long term performance of an High Temperature PEMFC based CHP system. The same authors performed another analysis [13] to evaluate the performance of the same system under partialization and power to heat shifting strategies. Hubert et al. [14] carried out a steady state modelling and optimization of a small heat and power PEMFC system, which is a part of EPACOP project installed in France. In this study, decreasing the natural gas consumption and increasing the heat recovery were considered as objective functions. Being a non conventional power generation technology, economic assessment of fuel cell based systems is of considerable importance [15,16]. Contreras et al. [17] performed an energetic and economic study on the utilisation of PEMFC based cogeneration systems in rural sector of Venezuela. Kamarudin et al. [18] carried out a profound study on economic evaluation of PEMFC systems. Guizzi et al. [19] performed an economic and energy performance assessment of a cogeneration system based on fuel cell designed for data centres.

Nižetić et al. [20] carried out a Levelised Cost of Energy (LCOE) analysis on an HT-PEM fuel cell based system supplying energy demand of a household in a Mediterranean climate. Niknam et al. [21] conducted an optimization and optimal planning study on a PEM fuel cell based combined heat, power and hydrogen production unit. Similar studies have also been carried out on tri-generation systems employing other types of fuel cells including solid oxide fuel cells (SOFCs). Ranjbar et al. [22] performed and energetic and exergetic assessment of a trigeneraton system based on SOFC technology. Joneydi Shariatzadeh et al. [23] performed an economic optimization study on a similar unit fed by biogas.

In the present work, a mathematical model of *Sidera30*, a natural gas fed residential micro cogeneration system manufactured by "ICI Caldaie", is first developed and different strategies are next proposed and implemented in order to facilitate addressing the intermittent loads.

Using the real geometries of the plant and employing kinetic models of the utilised catalysts, detailed mathematical models for the fuel processor reactors have been developed. The reactors models are subsequently validated using experimental data obtained from the plant. In order simulate the behaviour of the PEMFC stack, a detailed mathematical model has also been developed and validated using the experimental data provided by the manufacturer [24].

In the next step, the performance indices of the plant at normal operation are determined and two modifications for improving plant performance are proposed and applied. The obtained performance indices while applying the modifications are next determined and compared with the original ones.

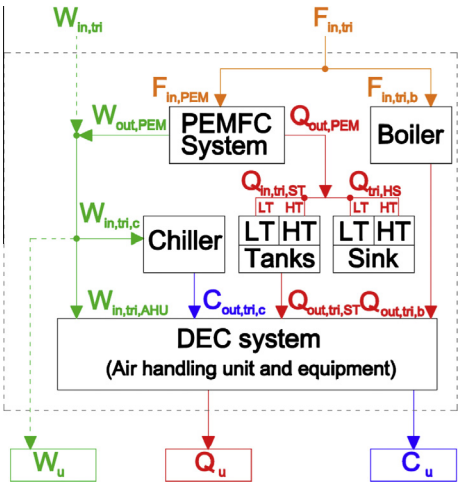


**Fig. 1.** A schematic view of the overall tri-generation plant.

Finally, the performance of the system at partial loads while operating at normal operation and with the proposed modifications is investigated and discussed.

## 2. Overall tri-generation plant description

Fig. 1 demonstrates the configuration of the overall tri-generative plant. As can be observed, the plant is composed of a PEMFC unit, a auxiliary boiler, a heat storage, a vapour compression chiller and a DEC air handling unit. The tri-generative system is designed to meet the thermal loads, which are extremely variable over the year. Accordingly, the amount of electrical power produced by the fuel cell system might not be enough to address electrical consumption of the chiller and air handling unit. Hence, if the fuel cells power output is higher than the electrical consumption of the chiller $W_{in,tri,c}$ and that of the air handling unit $W_{in,tri,\mathrm{AHU}}$, the surplus $W_u = (W_{out,\mathrm{PEM}} - W_{in,tri,c} - W_{in,tri,\mathrm{AHU}})$ will be useful output for on-site consumption. Instead, if $W_{out,\mathrm{PEM}}$ is not sufficient to meet electrical loads, the required electric power $W_{in,tri}$ is drawn from the national grid.

The thermal power generated by the fuel cell system is also accumulated in the heat storage and, once required, is provided to the air handling system. In case the power provided by the heat storage unit is not enough to address the thermal demand of the air handling unit, the thermal power produced by the boiler supplies the remaining required thermal power. On the other hand, in case the thermal power produced by the PEMFC system is more than the one required by the DEC system, the remaining thermal power is dispersed in the heat sink. It is also worth mentioning that, in the employed PEMFC system, thermal power is produced at two different temperature levels, the fact which explains the utilisation of two separate high temperature and low temperature tanks. The details of two thermal recovery circuits utilised in the PEMFC system are given in the next section.

## 3. Fuel cell system description

A schematic view of the *Sidera30* plant is demonstrated in Fig. 2. The feeding natural gas is mixed with the high pressure steam inside the ejector and the high pressure mixture of steam and methane is introduced into the Steam Methane Reforming (SMR) reactor, in which it is partly converted into hydrogen and carbon monoxide. In the next step, the generated syngas enters the pre Water Gas Shift (WGS) heat exchanger in which its temperature is decreased. The cooled syngas then enters the WGS reactor, in which part of the generated CO will be converted into $H_2$ and $CO_2$. Afterwards, the syngas is further cooled down in the post WGS heat exchanger to be in a suitable temperature range required by the next reactor. The remained carbon monoxide is then reduced to an acceptable level in the Preferential Oxidation (PrOx) units. In each PrOx reactor, a part of the containing CO is burnt and enters the next reactor in which the syngas is first cooled down and then undergoes a preferential oxidation reaction. In the actual operating condition of the plant, the syngas leaving the last PrOx reactor includes only 2 ppm of CO. The produced syngas is cooled down again in the pre fuel cell heat exchanger to reach the operating temperature of the stack. The pre fuel cell heat exchanger is followed by a water trap, which retains the most of the condensed water. The syngas, which has loss part of its containing water, enter the anode side of the PEMFC stack. The anodic flow, after undergoing the electrochemical reaction within the stack, enters the burner in which the remaining hydrogen within the flow is burnt together with the added auxiliary methane.

In the other side, owing to the fact that the cathodic flow should be humidified, the compressed ambient air enters the quencher, where a specific amount of water is added to the air stream. The quenched air then enters the humidifier, where the humidity and the heat contained in the cathode outlet is partly recovered. The heated and humidified air is then introduced into the cathode. For the sake of clarity, the process in which the water undergoes in high and low pressure circuits is explained in the following sections.

### 3.1. High pressure water circuit

The high pressure water circuit is an open circuit in which the water is supplied from a tank. The input temperature of water is considered to be 30 °C. It is also assumed that the water is pressurized by the high pressure (HP) pump to 7.83 bars. The water exiting the HP pump is divided into two flows, going through the pre and post WGS heat exchangers. Both flows are mixed in the next step and the mixture subsequently enters the super heater, in which the energy content remaining in the flue gases is recovered to produce super heated steam, which is fed to the ejector.

### 3.2. Low pressure water circuit

The low pressure water circuit is a closed circuit which should supply the thermal demand of the system. As can be seen in Fig. 2, the water leaving the stack heat exchanger is divided into the flows which pass through the PrOx heat exchangers and the economizer. These flows are then mixed and enter the thermal user 1 where they can yield the heat which they have recovered. For the sake of simplification, the losses are assumed to be negligible so as to have a constant pressure of 2 bars in the whole circuit. A separate thermal circuit is also employed for the pre fuel cell heat exchanger in which the heat gained in this heat exchanger, where the temperature of the syngas is reduced to the suitable range for entering the stack, is supplied to thermal user 2.

## 4. Mathematical modelling

### 4.1. Fuel processor

As was previously explained in the plant description, the fuel processor is composed of the syngas production and purification units. The syngas production is the process of converting the natural gas, which is mainly composed of methane, into hydrogen and carbon monoxide, while purification processes are attempts to decrease the carbon monoxide content of the syngas. In *Sidera30*

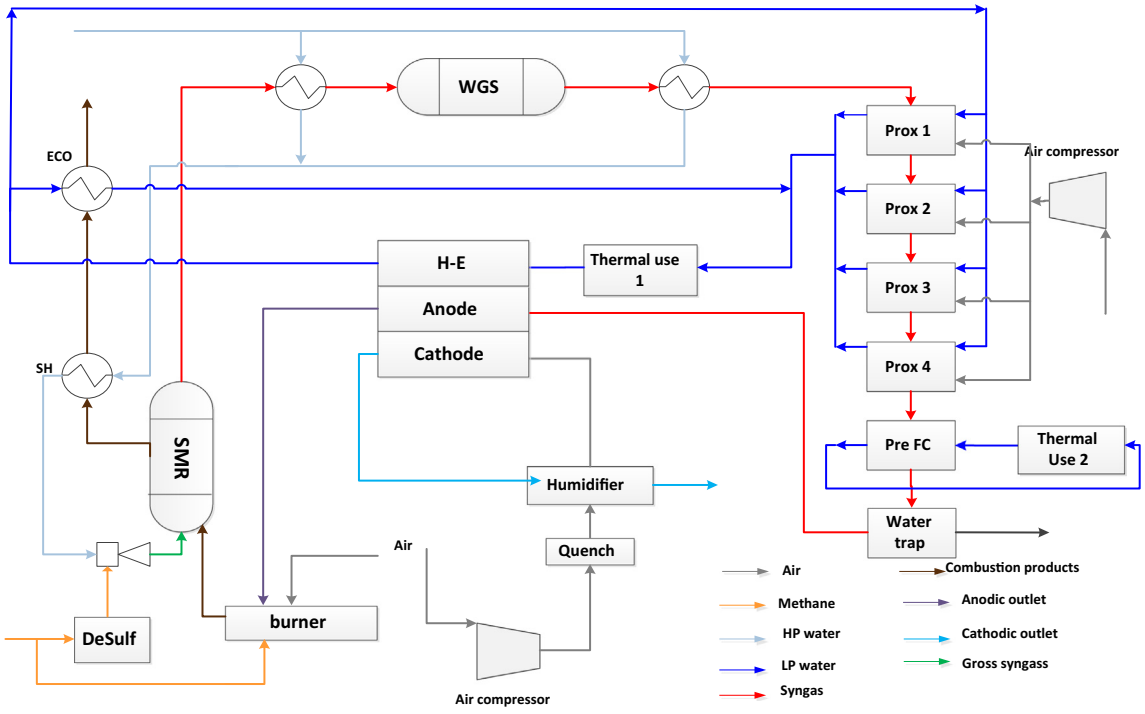


**Fig. 2.** Schematic view of the *Sidera30* plant.

plant, the SMR plays the role of syngas production while WGS and PrOx reactors are employed for accomplishing syngas purification.

*4.1.1. Steam methane reforming reactor*

Steam methane reforming is the conversion of natural gas (methane) with steam into a mixture of carbon oxides, hydrogen, unconverted steam and methane. In the present plant a tubular SMR is employed.

Xu and Froment [25] have developed a general and realistic Langmuir–Hinshelwood kinetic model for the steam reforming of methane using a Nickel based catalyst, considering the water gas shift reaction to occur in parallel with the steam reforming reactions. Accordingly, the following reactions are considered to take place in the reactor:

$$CH_4 + H_2O \Longleftrightarrow CO + 3H_2 \quad \text{Reaction} \tag{1}$$
$$CH_4 + CO_2 \Longleftrightarrow 2CO + 2H_2 \quad \text{Reaction} \tag{2}$$
$$CO + H_2O \Longleftrightarrow CO_2 + H_2 \quad \text{Reaction} \tag{3}$$

The corresponding kinetics equations are as follows:

$$r_1 = \frac{k_1}{P_{H_2}^{2.5}} \frac{P_{CH_4}P_{H_2} - P_{H_2}^3 P_{CO}/K_1}{DEN^2} \tag{4}$$
$$r_2 = \frac{k_2}{P_{H_2}} \frac{P_{CO}P_{H_2O} - P_{H_2}P_{CO_2}/K_2}{DEN^2} \tag{5}$$
$$r_3 = \frac{k_3}{P_{H_2}^{3.5}} \frac{P_{CH_4}P_{H_2O}^2 - P_{H_2}^4 P_{CO_2}/K_3}{DEN^2} \tag{6}$$

where

$$DEN = 1 + K_{CO}P_{CO} + K_{H_2}P_{H_2} + K_{CH_4}P_{CH_4} + \frac{K_{H_2O}P_{H_2O}}{P_{H_2}} \tag{7}$$
$$k_i = A(k_i) \cdot \exp[-E_i/(RT)], \quad \text{for } i = 1, \ldots, 3 \tag{8}$$
$$K_i = A(K_i) \cdot \exp[-\Delta G_i^\circ/(RT)], \quad \text{for } i = 1, \ldots, 3 \tag{9}$$
$$K_j = A(K_j) \cdot \exp[-\Delta H_j^\circ/(RT)], \quad \text{for } j = CH_4,\ H_2O,\ CO,\ H_2 \tag{10}$$

The kinetic parameters of the above reaction rates are extracted from Ref. [25], while the correlations proposed in Ref. [26] are employed for heat transfer calculations within the reformer.

*4.1.2. Water gas shift reactor*

The reaction taking place in the WGS reactor is the shift reaction:

$$CO + H_2O \Longleftrightarrow CO_2 + H_2 \quad \Delta H_{298}^\circ = -41.1 \text{ kJ mol}^{-1} \tag{11}$$

The applied mass and energy balance for the high temperature reactor elements are as follows [27]:

$$\frac{dx_{CO}}{dl} = \frac{\pi d_i^2}{4} \cdot \frac{r_{CO}}{F_{in}}, \quad x_{CO} = 0 \quad \text{at } l = 0 \tag{12}$$
$$\frac{dT}{dl} = \frac{-\Delta H_r}{C_p} \cdot \frac{\pi d_i^2}{4} \frac{r_{CO}}{F_{in}}, \quad T = T_{in} \quad \text{at } l = 0 \tag{13}$$

For the shift converter, according to Keiksi et al. [28], the kinetic equation for high temperature WGS with $Fe_3O_4$–$Cr_2O_3$ catalyst is:

$$r = k_0 \cdot \exp\left(\frac{-E_a}{RT}\right)(1-\beta)P_{CO}^{1.1}P_{H_2O}^{0.53} \tag{14}$$

where $E_\alpha$ = 95,000 kJ/mol is the activation energy, $ln\ (k_0)$ = 26.1 is pre-exponential factor and $\beta$ is the reversibility factor defined as:

$$\beta = \frac{1}{K}\frac{P_{CO_2}P_{H_2}}{P_{CO}P_{H_2O}} \tag{15}$$

*4.1.3. Preferential oxidation reactors*

Classically, in a CO preferential oxidation reactor the following reactions take place [29]:

$$CO + \frac{1}{2}O_2 \rightarrow CO_2 \quad \Delta H_{298}^\circ = -283.0 \text{ kJ mol}^{-1} \tag{16}$$
$$H_2 + \frac{1}{2}O_2 \rightarrow H_2O \quad \Delta H_{298}^\circ = -241.8 \text{ kJ mol}^{-1} \tag{17}$$

The kinetics of these two reactions have been modelled in the literature [30] using generalised empirical rate laws of the form:

$$R_C = k_C \exp\left(-\frac{E_C}{RT}\right)P_{CO}^a P_{O_2}^b \tag{18}$$
$$R_H = k_H\left(-\frac{E_H}{RT}\right)P_{O_2}^c \tag{19}$$

The corresponding kinetic constants of the preceding equations are extracted from Ref. [30].

### 4.2. PEM fuel cell stack

#### 4.2.1. Modelling methodology

The PEMFC stack employed in *Sidera30* plant is composed of 4 modules, each including 110 cells. A quasi 2D finite difference model has been developed to model a single channel. One coordinate of integration is considered along the channel, while the other integration coordinate is through MEA thickness.

The flow is considered to be equally divided between all channels with the same initial composition. Accordingly, the mass flow rate entering one single channel can be found as follows:

$$\dot{m}_{in} = \frac{\dot{M}}{N_{\text{modules}} N_{\text{cell}} N_{\text{ch}}} \tag{20}$$

where $N_{\text{modules}}$ is the number of modules, $N_{\text{cell}}$ is the number of cells per each module and $N_{\text{ch}}$ stands for the number of channel within a cell.

Infinitesimal elements are considered along channel length and governing electrochemical relations are solved to find the current density through the MEA at each element. The model is iteratively solved in order to get the desired average current density:

$$\frac{\int_0^L i(l)dl}{L} \cong \sum_{k=1}^{N_{\text{element}}} \frac{i^k \Delta l_k}{L} \cong \overline{i_{\text{exp}}} \tag{21}$$

The result is the stack voltage, determined by summing up the voltage of all the cells:

$$V_{\text{Stack}} = N_{\text{Mod}} N_{\text{cell}} V_{\text{cell}} \tag{22}$$

The utilised electrochemical relations are extensively explained in the following section.

Using the generated result for each element, the quantity of consumed hydrogen and oxygen in the stack can be evaluated by integrating these values along the length of a single channel and multiplying them by the number of channels and cells:

$$m_{\text{cons}} = \sum_{k=1}^{N_{\text{element}}} \frac{i^k \Delta l_k}{nF} W_{\text{ch}} N_{\text{ch}} N_{\text{cell}} N_{\text{mod}} \tag{23}$$

where $n$ is equal to 2 for $H_2$ and 4 for $O_2$, $i^k$ is the local current density at each element and $W_{\text{ch}}$ is the channel width.

Furthermore, in order to determine the flow rate of the water transported through the membrane of a single channel, an integration is performed through the MEA. Once the quantity of water transported through a single channel is determined, the total flow rate can be calculated by multiplying it by the number of channels and cells.

Considering the inlet anodic flow rate and composition and taking into account the determined quantity of consumed hydrogen and the water transport toward the anode, the flow rate and composition of the anodic outlet flow can be calculated.

Similarly, based on the inlet composition and flow rate, the consumed amount of oxygen and the water transported toward the cathode, the outlet flow rate and composition of the cathodic side is determined.

The power generated from the stack is simply calculated by multiplying the overall current of the stack by the voltage:

$$P_{\text{el}} = VI \tag{24}$$

where $V$ is the product of the voltage of a single cell multiplied by the number of cells and $I$ is the product of the current density and membrane area. The thermal loss from the stack can be found using the energy balance as follows:

$$Q_{\text{th}} = \dot{m}_{\text{H}_2,\text{cons}} \text{LHV}(\text{H}_2) - P_{\text{el}} \tag{25}$$

#### 4.2.2. Cell voltage

The actual voltage of the stack is determined as the difference between the ideal open circuit voltage and the losses occurring at the electrodes and in the electrolyte:

$$V = E_0 - \eta_a - \eta_c - \eta_{\text{ohm}} \tag{26}$$

The ideal open circuit voltage of the cell as a function of temperature is defined as [31]:

$$E_0 = 1.23 - 0.0009(T - 298) \tag{27}$$

#### 4.2.3. Cathodic activation voltage loss

The transport of oxygen trough the cathodic Gas Diffusion Layer (GDL) is described by Fick's law of diffusion. However, it should be taken into account that, since the presence of liquid water leads to a reduction in the local diffusivity owing to occupying of the pores, the mass diffusivity should be modified based on the calculated local water concentration. Accordingly the concentration of water at cathodic channel and the saturation concentration are determined. Hence, to consider this phenomenon, the model proposed in Ref. [32] has been adopted, where the effective diffusivity decreases as a function of the water liquid concentration:

$$D_{\text{eff}} = \begin{cases} D\left(\frac{T}{333}\right)^{1.75} & \text{FC} \leqslant 1 \\ \left(D - C_1\left(C_{(\text{H}_2\text{O})} - C_{\text{sat}}\right)^{(C_2)}\right)\left(\frac{T}{333}\right)^{1.75} & \text{FC} > 1 \end{cases} \tag{28}$$

where FC represents the ratio of the water concentration in the channel with respect to the saturation value and $C_1$ and $C_2$ are empirical constants derived from Ref. [32]. These relations provide a nonlinear diffusivity dependence on the water liquid concentration when the overall water concentration exceeds the water saturation value. The effective diffusivity is considered exponentially dependent on the temperature.

After calculating the oxygen concentration at electrode active sites, the cathodic activation loss can be calculated as follows:

$$\eta_c = \ln\left(\frac{i_{\text{cell}}}{i_{0,\text{ref}}} \frac{C_{\text{O}_2}^{\text{ref}}}{C_{\text{O}_2}^{\text{electrode}}}\right)^{\gamma} \frac{\text{RT}}{\alpha F} \tag{29}$$

where the kinetic parameters have been calibrated with respect to experimental data provided by the fuel cell manufacturer [24].

#### 4.2.4. Anodic activation voltage loss

In order to determine the hydrogen concentration on the anodic electrode and the inherent activation loss, a similar approach as utilised for the cathodic side should be employed. The issue which should be taken into account in the anodic side is the coverage of the catalyst by carbon monoxide. The model reported in Ref. [33] has been adopted, in which the current density is the sum of the current densities due to hydrogen and carbon monoxide. In this model it has been assumed that the catalyst layer has a uniform effective ionic conductivity and uniform effective diffusion coefficients both for hydrogen and carbon monoxide. The local generated kinetic ionic current densities, corresponding to both hydrogen and CO conversion, are expressed as equivalent A/cm$^2$ per geometric electrode area.

Accumulated ionic current densities of hydrogen and carbon monoxide range from zero at the backing interface to the total current density at the membrane interface.

The Nernst potential is a function of the hydrogen concentration, defined by the following correlation:

$$V_{\text{Nernst}} = \frac{\text{RT}}{2F} \log \frac{P_{\text{H}_2}}{P_{\text{ref}}} \tag{30}$$

The coverage factors of hydrogen and carbon monoxide can be found using the following equations, respectively:

$$\Theta_{\mathrm{H}} = \frac{k_{fh} P_{H_2}(1-\Theta_{\mathrm{CO}})}{k_{\mathrm{fh}}(b_{\mathrm{fh}} + P_{H_2}) + 2k_{\mathrm{eh}} \sinh\left(\frac{\eta_A + V_{\mathrm{Nernst}}}{b_h}\right)} \tag{31}$$

$$\Theta_{\mathrm{CO}} = \frac{k_{\mathrm{fc}} P_{\mathrm{CO}}(1-\Theta_{\mathrm{H}})}{k_{\mathrm{fc}}(b_{\mathrm{fc}} + P_{\mathrm{CO}}) + k_{\mathrm{ec}} \sinh\left(\frac{\eta_A + V_{\mathrm{Nernst}}}{b_c}\right)} \tag{32}$$

The current attributed to the carbon monoxide is determined by the CO coverage [23]; next, as the total current is already known, the current due to the hydrogen is calculated. This value, together with the $H_2$ coverage, is necessary for the anodic overpotential evaluation.

The anode parameters have been taken from Table 1 of Ref. [33] expect for the natural Tafel slope for CO electro-oxidation, $b_c$, which has been calibrated with respect to experimental data provided by the manufacturer [24].

$$\eta_A = b_h \sinh^{-1}\left(\frac{i_{H_2}}{2k_{\mathrm{eh}}\Theta_{\mathrm{H}}}\right) - V_{\mathrm{Nernst}} \tag{33}$$

#### 4.2.5. Ohmic voltage loss

In order to calculate the membrane proton resistance, which is strongly related to the hydration level, the water content profile within the membrane should be determined. Accordingly, the value of lambda ($\lambda$), which is the water content per each site of $SO_3^-$, should be calculated. The conductivity of the membrane is defined as a function of $\lambda$ and operating temperature using the following relation:

$$\sigma = (0.005139\lambda - 0.00326)\, e^{\left(1268\left(\frac{1}{303} - \frac{1}{T}\right)\right)} \tag{34}$$

The overall resistance of the membrane can be determined by integrating the conductivity through the thickness of the membrane:

$$R_m = \int_0^{S_{\mathrm{MEA}}} \frac{dx}{\sigma(\lambda)} \cong \sum_{k=1}^{N_{\mathrm{MEA}}} \frac{\Delta x_k}{\sigma(\lambda_k)} \tag{35}$$

The membrane resistance is summed up with the overall electrical resistance and the total ohmic loss is equal to:

$$\eta_R = (R_m + R_{bp})i \tag{36}$$

where $i$ represents the current density of the cell.

#### 4.2.6. Water transport

The water transport through the membrane is mainly due to electro-osmotic drag by proton transport and diffusion by water concentration gradient, while convection by hydraulic pressure gradient is neglected. The issue of drying of the membrane might take place at anode interface, while flooding may occur at the cathode. Hence, accurate determination of the transported water is necessary. In the present model, the reference flow of water toward the electrode is defined as:

$$N_{\mathrm{H_2O,ref}} = \frac{i}{2F} \tag{37}$$

and a parameter called $\alpha$ is defined as the ratio between the inlet water flow rate and the reference one, as reported in Ref. [34].

According to Ref. [34], the activity of the water at both anode and cathode electrodes is calculated, which yields the values of lambda at both sides:

$$\lambda_{\mathrm{elec}} = 0.043 + 17.81 a_{\mathrm{elec}} - 39.85 a_{\mathrm{elec}}^2 + 36 a_{\mathrm{elec}}^3 \tag{38}$$

The concentrations at saturation are derived from Ref. [35]. After obtaining the values of $\lambda$, the integration through the thickness of the membrane is performed by solving the differential equation (obtained from Ref. [36]) of the total flow of water due to electro-osmotic drag and diffusion:

$$N_{\mathrm{water}} = -D_w(\lambda_w)\nabla C_w + \frac{n_d(\lambda_w) i}{F} \tag{39}$$

where $D_w$ represents the mass diffusivity of the liquid water and $n_d$ is the number of molecules of water which are transported by a single proton. Both of these parameters are a function of the water content $\lambda_w$ and the following relations represent the dependence of these parameters on $\lambda_w$:

$$D_w = 4.1 \times 10^{-6}\left(\frac{\lambda_w}{25}\right)\left[1 + \tanh\left(\frac{\lambda_w - 2.5}{1.4}\right)\right] \tag{40}$$

$$\eta_d = \begin{cases} 1 & \lambda_w < 9 \\ 0.117\lambda_w - 0.0544 & \lambda_w \geqslant 9 \end{cases} \tag{41}$$

By replacing the last two relations in the Eq. (39), a new value for the water content at the cathode is found and compared to the one evaluated from Eq. (38) and the iteration continues until the difference between the two values approaches zero.

### 4.3. Auxiliary components

#### 4.3.1. Ejector

In order to model the ejector the thermodynamic model proposed by Eames et al. [37] has been employed. The employed model is a single phase thermodynamic model which is developed based on the isobaric mixing. In this model in order to simulate the behaviour of the ejector, energy conservation equation for the ejector's nozzle and the momentum conservation equation for the mixing section is first solved. Using a correlation based on the Mach numbers before and after the wave, the pressure change due to the shock wave is also considered. Finally, using the corresponding determined Mach number, the outlet pressure is obtained.

#### 4.3.2. Heat exchangers

An iterative LMTD method has been utilised to model the heat exchangers, in which the evaporation does not take place.

In order to determine the external convective heat transfer coefficient, the Churchill–Bernstein relation for cross flow heat exchange over tubes is employed [38,39]:

$$Nu_D = 0.3 + \frac{0.62 Re_D^{1/2} Pr^{1/3}}{\left[1 + \left(\frac{0.4}{Pr}\right)^{2/3}\right]^{1/4}} \left[1 + \left(\frac{Re_D}{282,000}\right)^{5/8}\right]^{4/5} \tag{42}$$

This relation is valid for the conditions in which $RePr > 0.2$ and the properties are evaluated at film temperature.

For calculation of the internal heat transfer coefficient, Gnielinski [38] equation is utilised:

$$Nu_D = \frac{(f/8)(Re_D - 1000)Pr}{1 + 12.7(f/8)^{1/2}(Pr^{2/3} - 1)} \tag{43}$$

This relation is valid if $5 < Pr < 3000$, $3000 < Re_D < 5 \cdot 10^6$, the flow is fully developed and the ratio between the length and diameter of the tube is greater than 10. The properties are evaluated at an average temperature. It should also be noted that in the cases in which the flow is laminar and fully developed the Nusselt is equal to 4.36.

The friction factor ($f$) is evaluated using the following equation:

$$f = (0.79 \log Re_D - 1.64)^{-2} \tag{44}$$

## 5. Model validation

### 5.1. Fuel processor validation

The validation procedure is carried out by imposing the mass flow rates of process and auxiliary fuel and the water flow rates in both circuits in the operating condition of the plant. Using the mentioned parameters in the developed model, the composition and the temperature of the syngas in different points is determined. Tables 1 and 2 demonstrate the comparison between the values obtained by the model and the experimental data.

It is worth mentioning that, owing to the uncertainty on the catalyst density within the reactors, a calibration procedure has been carried out on this parameter and the resulting values are consistent with the state of the art industrial values. Nevertheless, considering the data confidentiality agreement with the industrial partner the obtained calibrated values are not given.

### 5.2. Stack model validation

In order to investigate the validity of the developed stack model in different operating conditions, given in Table 3, the resulting current density–voltage curve has been compared with the experimental data provided by the stack manufacturer [24]. Fig. 3 illustrates the comparison between the simulated and measured stack performance with different anode CO concentrations, equal to 0 and 10 ppm, respectively. The model reproduces the experiments with good accuracy and therefore all the main physical phenomena are correctly described. Table 4 reports the main assumed and fitted model parameters, whose values are coherent with those reported in the literature.

**Table 1**
Outlet dry molar fractions of the SMR and WGS reactors obtained from the model and the provided experimental data.

| Dry molar fraction | $CH_4$ | $H_2$ | CO | $CO_2$ | $N_2$ |
|---|---|---|---|---|---|
| SMR outlet (experimental) | 0.0452 | 0.749 | 0.051 | 0.151 | 0.0047 |
| SMR outlet (model) | 0.0528 | 0.745 | 0.0478 | 0.1504 | 0.00418 |
| WGS outlet (experimental) | 0.045 | 0.753 | 0.012 | 0.1856 | 0.0044 |
| WGS outlet (model) | 0.0508 | 0.754 | 0.00865 | 0.182 | 0.00403 |

**Table 2**
Outlet temperatures of the fuel processor reactors and superheater obtained from the model and the provided experimental data.

| Parameter | Model (°C) | Experimental (°C) |
|---|---|---|
| Syngas temperature at SMR outlet | 577 | 590 |
| Syngas temperature at WGS outlet | 339 | 331 |
| Steam temperature at superheater outlet | 535 | 527 |

**Table 3**
Operating conditions utilised for model validation at 61 °C.

| Reactants | Current (A) | | | |
|---|---|---|---|---|
| | 15 | 30 | 60 | 120 |
| *Anode side* | | | | |
| Stoichiometry | 6.3 | 3.4 | 2.2 | 1.6 |
| Inlet pressure (kPa) | 115 | 116 | 131 | 157 |
| *Cathode side* | | | | |
| Stoichiometry | 5.1 | 2.4 | 1.8 | 1.8 |
| Inlet pressure (kPa) | 108 | 110 | 117 | 135 |

## 6. Results and discussion

### 6.1. Full load performance analysis

#### 6.1.1. Performance analysis of the plant

The operating parameters which have been considered in the present analysis are given in Table 5. Taking into account the interconnection between the components of the plant, an iterative procedure has been employed in order to obtain the converged results of the performance of the system. The obtained results, shown in Table 6, demonstrate that the electrical power of 20.9 kW is produced, while 52.3 kW of total thermal power can be gained from the system. Accordingly, electrical and thermal efficiencies of 21.4% and 53.7% are achieved, respectively.

#### 6.1.2. Performance analysis of the plant with modification 1

As the first modification, in order to decrease the amount of the required fuel to be provided to the burner, the inlet air fed to the burner is preheated using the outlet combustion gases leaving the super-heater. In this way, the inlet temperature of the air is considerably boosted, the fact which consequently leads to obtaining the same burner outlet temperature while using less fuel fed to the burner. In this context, as demonstrated in Fig. 4, the ambient

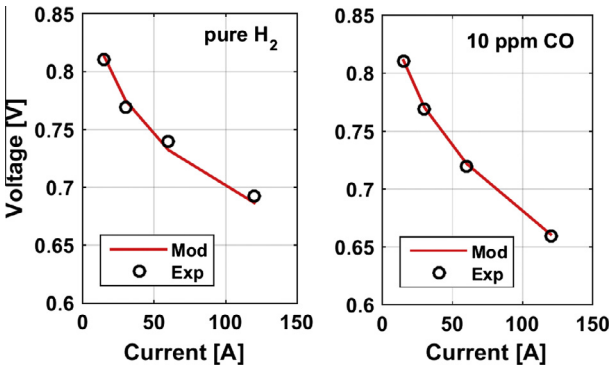


**Fig. 3.** Comparison between simulated and measured stack performance.

**Table 4**
Assumed and fitted model parameters.

| Parameter | Value | | |
|---|---|---|---|
| $b_c$ | 0.078 | V | Calibrated |
| $\alpha$ | 1 | | Assumed |
| $i_{0,ref}$ | 3.9e-5 | A $cm^{-2}$ | Calibrated |
| $\gamma$ | 0.8 | | Assumed |
| $D_{GDL,O2}$ | 0.041 | $cm^2$ $s^{-1}$ | Calibrated |
| $N_{modules}$ | 4 | | Manufacturer |
| $N_{cell}$ | 110 | | Manufacturer |
| $N_{ch}$ | 20 | | Assumed |
| $L$ | 72 | cm | Assumed |

**Table 5**
The operating parameters of the plant without modification.

| Operative Condition | Value |
|---|---|
| Steam to carbon ratio (S/C) | 4.5 |
| Auxiliary to process flow rate ratio | 0.175 |
| Anodic stoichiometric ratio | 1.6 |
| Cathodic stoichiometric ratio | 2 |
| Current density (A $cm^{-2}$) | 0.2 |
| Combustor outlet temperature (°C) | 920 |
| Cell temperature (°C) | 66 |

**Table 6**
Performance indices of the plant.

| Performance index | W/O modifications | Modification 1 | Modification 2 |
|---|---|---|---|
| Generated net electrical power (kW) | 20.90 | 20.90 | 23.30 |
| Generated total thermal power (kW) | 52.33 | 40.30 | 40.30 |
| Electrical efficiency (%) | 21.44 | 24.20 | 26.98 |
| Thermal efficiency (%) | 53.68 | 46.67 | 46.67 |
| First law efficiency (%) | 75.12 | 70.88 | 73.67 |

air is first introduced into a recuperator, where it exchanges heat with the flue gases coming out of the super-heater. However, it should be mentioned that using this approach, the available heat for the thermal user will be reduced as the temperature of the flue gases entering the economizer is reduced. As can be seen in Table 6, due to the decrement in the required fuel while keeping the electrical generation constant, the electrical efficiency is increased from 21.4% to 24.2%. It can also be observed that, owing to the lower heat gain in the economizer, the thermal efficiency is reduced from 53.7% to 46.7%.

*6.1.3. Performance analysis of the modified plant with modification 2*

In the second modification, which includes also the modification 1, to improve the performance of the plant in terms of both electrical and thermal efficiency, some of the components in the plant are going to be replaced by properly optimised components with higher efficiencies and reduced losses. In this regard, relying on manufacturers suggestions, the isentropic efficiency of the cathodic and PrOx compressors have been increased from 0.6 to 0.8, the inverter efficiency has been increased from 0.9 to 0.94, while the amount of the other auxiliary losses in the plant have been reduced to one third of the original value. As can be observed in Table 6, applying the mentioned modifications results in increasing the electrical efficiency of the plant, from 24.2% to 27.0% which demonstrates the corresponding available room for improvement.

*6.2. Performance analysis of the system at partial loads*

In the next step, the performance of the plant while operating at partial loads is investigated. Estimating the plant's behaviour at partial loads, provides the possibility of determining the performance of the plant while addressing the load profiles, as carried out in part B of this article [34]. Accordingly, the mass flow rate of the injected fuel to the steam reformer is progressively decreased and the performance of the system in terms of thermal and electrical output and efficiency have been simulated. Fig. 5 displays the variations in the electrical and thermal power output of the plant with fuel partialization up to 60% of the initial value. As it can be seen in this figure, the thermal output is steadily

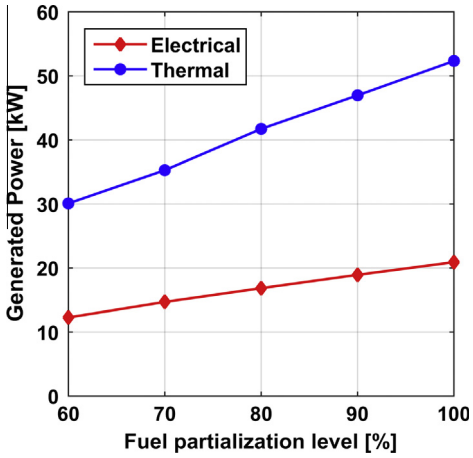


**Fig. 5.** Simulated thermal and electrical output at different fuel partialization levels.

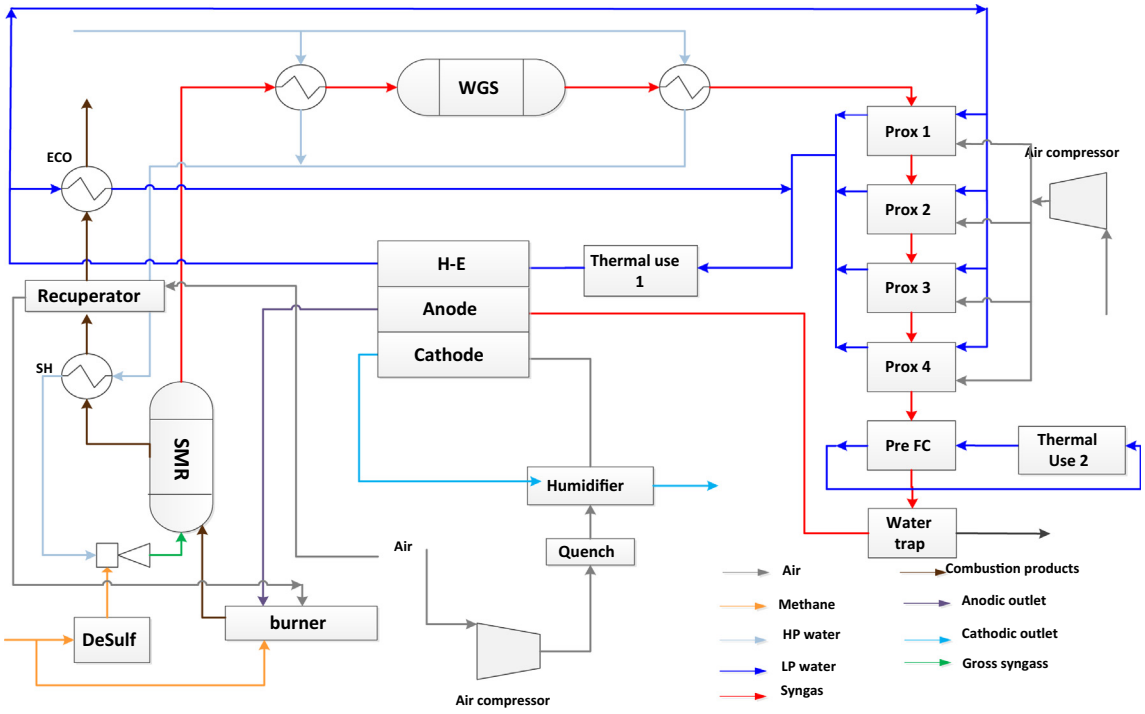


**Fig. 4.** Schematic view of the *Sidera30* plant with modification 1.

**Table 7**
Electrical and thermal efficiency at different partialization.

| Load (%) | $\eta_{el}$ (%) | $\eta_{th}$ (%) |
|---|---|---|
| 100 | 21.43 | 53.68 |
| 90 | 21.57 | 53.52 |
| 80 | 21.58 | 53.49 |
| 70 | 21.59 | 51.69 |
| 60 | 21.60 | 51.44 |

**Table 8**
Electrical efficiency at different partialization level with and without modifications.

| Load | 100% | 90% | 80% | 70% | 60% |
|---|---|---|---|---|---|
| W/O modification | 21.43% | 21.57% | 21.58% | 21.59% | 21.60% |
| Modification 1 | 24.20% | 24.25% | 24.33% | 24.39% | 24.50% |
| Modification 2 | 26.98% | 27.03% | 27.13% | 27.34% | 27.54% |

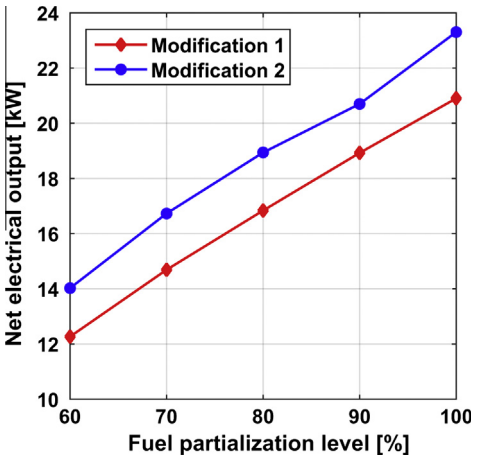


**Fig. 6.** Simulated electrical output at different fuel partialization levels.

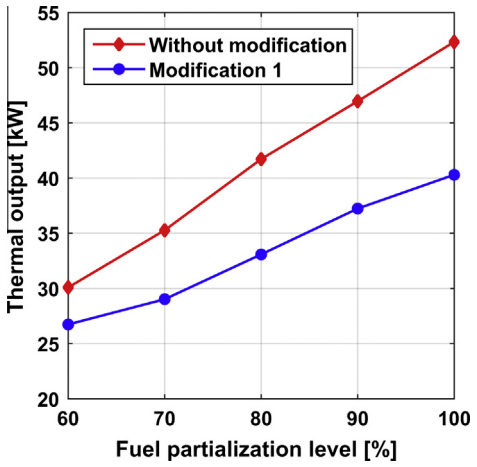


**Fig. 7.** Simulated thermal output at different fuel partialization levels.

decreasing from 52.3 kW to 30.1 kW, while the electrical generation is diminished from 20.9 kW at full load condition down to 12.3 kW at 60%.

Considering the fact that in the present analysis the design of the system (fuel processor and stack geometries) is fixed and only the provided fuel flow rate is being reduced, the electrical and thermal performance of the system will be inevitably different from the full load condition values. As it can be seen in Table 7, fuel partialization results in a negligible increment in the electrical efficiency of the entire system, while it diminishes the thermal efficiency. For instance, by decreasing the fuel input to 60% of the initial value, the electrical efficiency is nearly constant, while the thermal efficiency is reduced from 53.7% to 51.4%. Almost constant trend of the electrical efficiency is owing to the compromise between the increasing negative effect of auxiliaries on electrical efficiency at partial loads and the conversion improvement in the reformer.

Regarding the thermal efficiency's behaviour, it can be observed that while operating at partial loads less hydrogen is injected to the stack leading to lower current densities and accordingly higher voltages. The fact which in turn reduces the thermal generation of the stack and consequently the overall thermal efficiency of the system will be reduced.

### *6.3. Performance analysis of the system at partial loads with modifications*

In order to study the room for improving the plant's performance while addressing intermittent load profile, the performance of the system at partial loads while applying the mentioned modifications is studied.

Table 8 demonstrates the electrical efficiency of the system obtained at different fuel partialization levels while applying the modifications. As can be seen in this table, the same behaviour as the one of the plant without modification is observed and the electrical efficiency of the system is almost constant.

Fig. 6 shows the net electrical output of the plant with the first and second modifications while operating at partial loads. It can be seen that the net electrical output of the system with the first modification is reduced from 20.9 kW to 12.3 kW with the first modification while the corresponding value is decreased from 23.3 kW to 14.0 kW with the second modification. Fig. 7 demonstrates the overall thermal generation profile of the plant without modification and with modification 1 while operating at partial loads. The thermal generation of the plant with the first modification is decreased from 40.3 at full load condition down to 26.7 kW at 60%. Table 9 demonstrates the thermal power obtained in thermal use 1 (HT) and thermal use 2 (LT) at different partialization levels without modification and with modification 1. The outlet temperature of water leaving thermal use 2 has also been given. The inlet temperature of water entering thermal use 2 is 40 °C while the inlet and outlet temperature of water entering and leaving thermal use 1 is kept constant and equal to 61 °C and 69 °C respectively. It is worth mentioning that while applying the modification 1, the syngas composition and temperature is kept almost constant; hence, the thermal power gained at thermal use 2 (LT) and the corresponding outlet temperature does not change.

**Table 9**
Thermal power and temperature outlet of thermal use 1 and 2 at partial loads.

| Load (%) | $\dot{Q}_{\text{thermal use 1(HT)}}$ (kW) W/O modification | $\dot{Q}_{\text{thermal use1(HT)}}$ (kW) modification 1 | $\dot{Q}_{\text{thermal use 2(LT)}}$ (kW) | $T_{\text{outlet thermal use 2}}$ (°C) |
|---|---|---|---|---|
| 100 | 40.7 | 28.7 | 11.6 | 49 |
| 90 | 36.5 | 26.5 | 10.5 | 51 |
| 80 | 32.4 | 23.7 | 9.4 | 53 |
| 70 | 28.4 | 20.8 | 8.3 | 56 |
| 60 | 24.3 | 19.5 | 7.1 | 59 |

The corresponding results can be employed in a further study to analyse the overall performance of the system while meeting the thermal load.

## 7. Conclusion

In the present article, a detailed physically based mathematical model of *Sidera30*, a residential micro-cogeneration system based on PEMFC, has been first developed and validated.

Next, in order to boost the electrical efficiency of the system, two modifications have been proposed. By applying the first modification, in which the plant configuration has been modified and an air pre-heater is employed, the electrical efficiency of the plant is increased from 21.4% to 24.2%. In the second modification, the performance of the plant while employing more efficient compressors and inverter is investigated to estimate the available room for improvement. It has been demonstrated that by applying the mentioned modifications on the plant with modified configuration, the electrical efficiency can be improved up to 27.0%.

In the next step, the performance of the plant, with and without the mentioned modifications, while operating at partial loads, has been studied and the corresponding performance indices have been reported, demonstrating to remain almost constant during power reduction. The obtained results permit to investigate the overall performance addressing variable thermal demand profile, as carried out for a tri-generative plant in the part B [34].

## Acknowledgments

Funding for this work from Italian Cassa Conguaglio Sistema Elettrico under Agreement No. 6562 is acknowledged (project STAR—Sidera Trigenerazione Alto Rendimento). The authors would also like to thank ICI Caldaie S.p.A. for providing technical support.

## References

[1] Ferguson A, Ismet Ugursal V. Fuel cell modelling for building cogeneration applications. J Power Sources 2004;137:30–42.
[2] Rinaldi F, Marchesi R. Polimeric electrolyte membrane fuel cells: characterization test under variable temperature and relative humidity conditions. J Fuel Cell Sci Technol 2007;4:231–7.
[3] Radulescu M, Lottin O, Feidt M, Lombard C, Le Noc D, Le Doze S. Experimental and theoretical analysis of the operation of a natural gas cogeneration system using a polymer exchange membrane fuel cell. Chem Eng Sci 2006;61:743–52.
[4] Ersöz A. Investigation of hydrocarbon reforming processes for micro-cogeneration systems. Int J Hydrogen Energy 2008;33:7084–94.
[5] Calise F, Ferruzzi G, Vanoli L. Transient simulation of polygeneration systems based on PEM fuel cells and solar heating and cooling technologies. Energy 2012;41:18–30.
[6] Obara SY, Tanno I. Study on capacity optimization of PEM fuel cell and hydrogen mixing gas-engine compound generator. Int J Hydrogen Energy 2007;32:4329–39.
[7] Obara SY. Discharge characteristic of PEM-FC/hydrogen-gas-engine hybrid cogeneration. Int J Hydrogen Energy 2007;32:819–31.
[8] Nagata Y. Quantitative analysis of $CO_2$ emissions reductions through introduction of stationary-type PEM-FC systems in Japan. Energy 2005;30: 2636–53.
[9] Hwang JJ, Zou ML. Development of a proton exchange membrane fuel cell cogeneration system. J Power Sources 2010;195:2579–85.
[10] Jovan V, Perne M, Petrovčič J. An assessment of the energetic flows in a commercial PEM fuel-cell system. Energy Convers Manage 2010;51:2467–72.
[11] Najafi B, Haghighat Mamaghani A, Baricci A, Rinaldi F, Casalegno A. Mathematical modelling and parametric study on a 30 kWel high temperature PEM fuel cell based residential micro cogeneration plant. Int J Hydrogen Energy 2015;40:1569–83.
[12] Najafi B, Haghighat Mamaghani A, Rinaldi F, Casalegno A. Long-term performance analysis of an HT-PEM fuel cell based micro-CHP system: operational strategies. Appl Energy 2015;147:582–92.
[13] Najafi B, Haghighat Mamaghani A, Rinaldi F, Casalegno A. Fuel partialization and power/heat shifting strategies applied to a 30 kWel high temperature PEM fuel cell based residential micro cogeneration plant. Int J Hydrogen Energy 2015;40:14224–34. http://dx.doi.org/10.1016/j.ijhydene.2015.08.088.
[14] Hubert C-E, Achard P, Metkemeijer R. Study of a small heat and power PEM fuel cell system generator. J Power Sources 2006;156:64–70.
[15] Haghighat Mamaghani A, Najafi B, Shirazi A, Rinaldi F. 4E analysis and multi-objective optimization of an integrated MCFC (molten carbonate fuel cell) and ORC (organic Rankine cycle) system. Energy 2015;82:650–63.
[16] Mamaghani AH, Najafi B, Shirazi A, Rinaldi F. Exergetic, economic, and environmental evaluations and multi-objective optimization of a combined molten carbonate fuel cell-gas turbine system. Appl Therm Eng 2015; 77:1–11.
[17] Contreras A, Posso F, Guervos E. Modelling and simulation of the utilization of a PEM fuel cell in the rural sector of Venezuela. Appl Energy 2010;87:1376–85.
[18] Kamarudin SK, Daud WRW, Som AMd, Takriff MS, Mohammad AW. Technical design and economic evaluation of a PEM fuel cell system. J Power Sources 2006;157:641–9.
[19] Guizzi GL, Manno M. Fuel cell-based cogeneration system covering data centers' energy needs. Energy 2012;41:56–64.
[20] Nižetić S, Tolj I, Papadopoulos AM. Hybrid energy fuel cell based system for household applications in a Mediterranean climate. Energy Convers Manage 2015;105:1037–45.
[21] Niknam T, Bornapour M, Gheisari A. Combined heat, power and hydrogen production optimal planning of fuel cell power plants in distribution networks. Energy Convers Manage 2013;66:11–25.
[22] Ranjbar F, Chitsaz A, Mahmoudi SMS, Khalilarya S, Rosen MA. Energy and exergy assessments of a novel trigeneration system based on a solid oxide fuel cell. Energy Convers Manage 2014;87:318–27.
[23] Joneydi Shariatzadeh O, Refahi AH, Rahmani M, Abolhassani SS. Economic optimisation and thermodynamic modelling of SOFC tri-generation system fed by biogas. Energy Convers Manage 2015;105:772–81.
[24] Ballard Mark9 SSL fuel cell stack catalogue; 2008.
[25] Xu J, Froment GF. Methane steam reforming, methanation and water-gas shift: I. Intrinsic kinetics. AIChE J 1989;35:88–96.
[26] Pantoleontos G, Kikkinides ES, Georgiadis MC. A heterogeneous dynamic model for the simulation and optimisation of the steam methane reforming reactor. Int J Hydrogen Energy 2012;37:16346–58.
[27] Rajesh JK, Gupta SK, Rangaiah GP, Ray AK. Multi-objective optimization of industrial hydrogen plants. Chem Eng Sci 2001;56:999–1010.
[28] Keiski RL, Salmi T, Niemistö P, Ainassaari J, Pohjola VJ. Stationary and transient kinetics of the high temperature water-gas shift reaction. Appl Catal A 1996;137:349–70.
[29] Baughman AC, Huang X, Martin LL. Evaluating kinetic models for preferential CO-oxidation catalysts using optimization-based parameter estimation. J Power Sources 2012;210:402–8.
[30] Zhou S, Yuan Z, Wang S. Selective CO oxidation with real methanol reformate over monolithic Pt group catalysts: PEMFC applications. Int J Hydrogen Energy 2006;31:924–33.
[31] Spiegel. PEM fuel cell modeling and simulation using MATLAB. Elsevier; 2008.
[32] Casalegno Bresciani, Groppi Marchesi. Flooding of the diffusion layer in a polymer electrolyte fuel cell. J Power Sources 2011;196:10632–9.
[33] Springer Rockward, Zawodzinski Gottesfeld. Model for Polymer electrolyte fuel cell operation on reformate feed. J Electrochem Soc 2001;148:A11–23.
[34] Chen Peng. A thermodynamic model of membrane humidifiers for PEM fuel cell humidification control. J Dyn Syst Meas Contr 2005;127:424–32.
[35] Handbook of chemistry and physics 53ed CRC1972.
[36] Kulikovsky A. Analytical modelling of fuel cells. Amsterdam: Elsevier; 2010.
[37] Li, He, Wang. Progress of mathematical modeling on ejectors. Renew Sustain Energy Rev 2009;13:1760–80.
[38] Fundamentals of heat and mass transfer, 6th ed. Wiley India Pvt. Limited; 2010.
[39] Churchill SW, Bernstein M. A correlating equation for forced convection from gases and liquids to a circular cylinder in crossflow. J Heat Transfer 1977;99: 300–6.